Explicit Fixed-Point Computation of Nonlinear Delay-Free Loop Filter Networks

Federico Fontana, *Senior Member, IEEE,* and Enrico Bozzo

Abstract

An iterative method is proposed for the explicit computation of discrete-time nonlinear filter networks containing delay-free loops. The method relies on a fixed-point search of the signal values at every temporal step. The formal as well as numerical properties of fixed-point solvers delimit its applicability: on the one hand the method allows for a reliable prediction of the frequency rates where the simulation is stable; on the other hand its straightforward applicability is counterbalanced by low speed of convergence. Especially in presence of specific nonlinear characteristics, the use of a fixed-point search is limited if the real-time constraint holds. For this reason the method becomes useful especially during the digital model prototyping stage, as exemplified while revisiting a previous discrete-time realization of the voltage-controlled filter aboard the EMS VCS3 analogue synthesizer. Further tests conducted on a digital ring modulator model support the above considerations.

Index Terms

Digital delay-free loop, nonlinear filter network, fixed-point method, voltage-controlled filter, ring modulator.

I. Introduction

The Delay-free loop (DFL from now on) problem appears when a digital filter network models one or more loopbacks containing no delay units along their path. Fig. 1(a) illustrates the problem through a simple example: in that network, $c(\cdot)$ is a discrete-time transfer characteristic in which no digital delay units can be factored out. Since the output $v[n]$ from the filter block propagates

F. Fontana and E. Bozzo are with the Department of Mathematics, Computer Science and Physics, University of Udine, Udine, 33100 Italy e-mail: {federico.fontana,enrico.bozzo}@uniud.it.

Draft Manuscript. Official version available at https://ieeexplore.ieee.org/document/8385118/

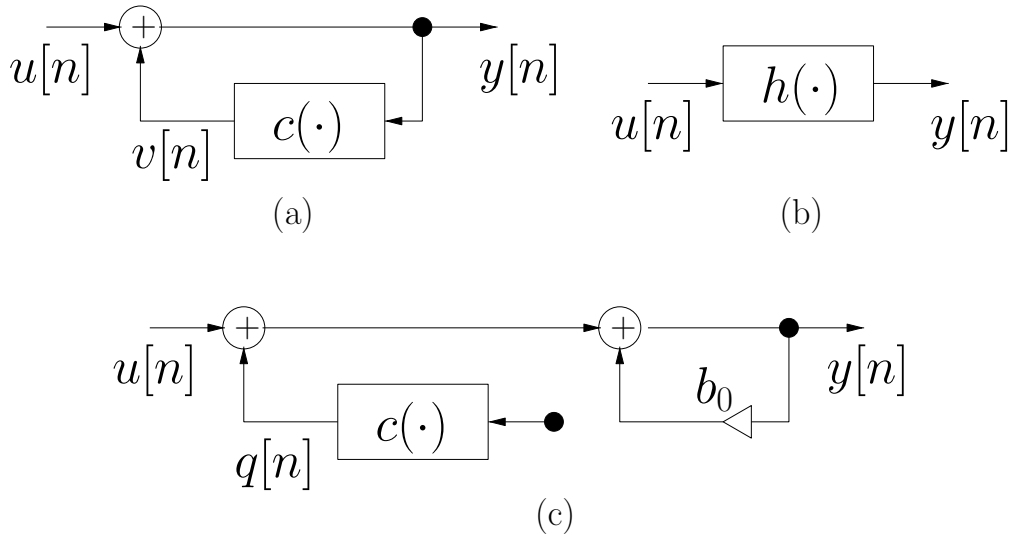

Fig. 1. Delay-free loop (a). Network-equivalent transfer function, linear case (b). Explicit computation of the delay-free loop, linear case (c).

instantaneously to the input of the same block after summation with $u[n]$, there is no explicit procedure allowing for the computation of the network.

If the block is linear then the output $y[n]$ from the network can be computed by convolution with an equivalent recursive filter which is linear in its turn, and incorporates the DFL as in Fig. 1(b) [1]: $y[n] = u[n] + (c * y)[n] = (h * u)[n]$. However, when modeling sound processing systems in the digital domain two situations can make this solution respectively unfeasible or undesirable. The first situation concerns cases in which $c(\cdot)$ is nonlinear. Secondly, even if the transfer characteristic is linear nevertheless it may vary in time depending on parameters which, once mapped onto the coefficients of the equivalent filter, can cause inaccuracy or instability during the computation. This second situation in particular affects digital realizations of analog processors, whose control parameters are often heavily tweaked by musicians through manual operation or use of specific driving signals.

Härmä first proposed an explicit solution of the linear DFL problem [2]. By expressing $v[n]$ as a linear superposition of a term $q[n]$ depending on past input values and another term $b_0 y[n]$ depending on the current input value to the filter block, he was able to reduce the DFL to a minimal loop structure computing only the instantaneous effects of the feedback in the network, as illustrated in Fig. 1(c). That loop acts as a simple multiplier by $(1 - b_0)^{-1}$. This solution has permitted the realization of recursive [3] including "warped" [4] filter realizations, magnitude-

complementary parametric equalizers [5], and an accurate linear model of the Moog voltage-controlled filter (VCF from here on) [6]. All such realizations proved to be robust and precisely responsive to online parametric control; in the meantime they preserved the structural aspects of the original filter model, particularly the direct access to the control parameters. A multi-dimensional solution of the DFL problem, applicable to any network of linear filters, allowed for the realization of "warped" finite-difference time-domain schemes characterized by having low wave dispersion [7].

The proposed solution, however, gives a partial answer to situations in which the DFL is nonlinear. Using the same decomposition proposed by Härma, Zavalishin came to an explicit solution of the linear DFL problem furthermore scalable to an implicit method for DFL structures containing a saturating nonlinearity [8], he later used to model analog structures including transistor and diode ladders that are core modules of the VCF [9]. Berners and Abel discretized arbitrary DFL networks of linear filters, exemplifying also with a parametric system and including memoryless nonlinearities in the loops [10]. More in general, an extension to nonlinear filter networks of the aforementioned decomposition again expresses the output as a superposition between a term depending on past input values and another term depending on the input at step n. Yet, the computation of the latter requires to solve an equation containing a multidimensional function $\boldsymbol{f}$ of the nonlinear transfer characteristics appearing in the network [11]:

$$\boldsymbol{v}_N[n] = \boldsymbol{f}\big(\boldsymbol{v}_N[n] + \boldsymbol{W}_N\boldsymbol{u}_N[n] + \boldsymbol{W}_L\boldsymbol{v}_L[n], \boldsymbol{p}\big), \tag{1}$$

in which the unknown array $\boldsymbol{v}_N[n]$ collects the outputs from the nonlinear blocks, $\boldsymbol{W}_N$ weighs the external signal contributions $\boldsymbol{u}_N[n]$ to the same blocks, $\boldsymbol{W}_L$ weighs simultaneous contributions $\boldsymbol{v}_L[n]$ from the linear blocks belonging to the network, and finally $\boldsymbol{p}$ accounts for the dependency of $\boldsymbol{f}$ on past values if there are nonlinear transfer characteristics with memory in the network. Although quite general, such an approach proved successful in simulating the Chua-Felderhoff RLC circuit, a distributed model of circadian oscillations [11], and a digital simulation of the Dolby B system [12]. A similar approach was proposed by Yeh *et al.*, who simulated guitar distortion and vacuum tube amplifiers also optimizing the access to pre-computed solutions of the nonlinear equation (1) through the use of netlists and multidimensional linear interpolation [13], [14]. Both approaches rely on the K-method [15] that put a firm basis for the computation of nonlinear DFLs with application to impact sound synthesis [16], particularly for the simulation of hammer-string interactions in piano instrument models [17].

The search for efficient discrete-time methods for the simulation of nonlinear analog circuits has led to a broad family of numerical techniques with various degrees of generality, some of which avoid the definition of a filter network and rather model the system under inspection as a wave-based, state-space, or other structure.

The wave-based approach includes Block Compiler, an early automatized procedure for the computation of nonlinear circuits such as vacuum tubes based on Wave Digital Filters [18]; the WT method, organizing nonlinear Wave-Digital structures in a "wave tableau" with application to RLC circuits, damped oscillators, and in general Wave Digital Networks containing one nonlinear element [19]; recent Wave Digital Filter adaptors applicable to arbitrary topologies, which have notably expanded the range of linear circuits admitting a Wave Digital Network model [20].

The state-space approach has been enriched with recent methods too, adding versatility [21], efficiency [22] and modularity [23] to previous state-space representation frameworks [13], [11]. Other approaches include the Functional Transformation Method [24], applied to nonlinear fret-string interactions and to room acoustic simulation; a Port-Hamiltonian approach preserving the energy properties of the original analog audio circuit, that successfully simulated a diode clipper, a common-emitter bipolar-junction transistor amplifier, and a wah pedal [25]; a linearization method reproducing the system response around a static operating point through IIR filters, which modeled the Moog VCF efficiently [26]; a method for modeling nonlinear wave digital elements using the Lambert function [27]. In parallel to them, a number of successful solutions have been proposed having different levels of generality (see for instance [28], [29], [30], [31], [32]).

A. Scope and structure of the paper

This paper investigates whether a set of difference equations resulting from the discretization of an ordinary differential equation system can be computed directly, once the difference equations are expressed in the form of a nonlinear DFL network. The idea to compute a filter network *as it is* makes the development of a musical circuit model almost immediate. On the other hand it restricts the choice of numerical methods to solvers which must not transform the network, with consequently expected lack of efficiency of the solution.

An early intuition behind this idea can be appreciated by looking back to Fig. 1. Instead of calculating the output as $y[n] = (u[n] + q[n])/(1 - b_0)$ if $b_0 \neq 1$, hence realizing the network in Fig. 1(c), $y[n]$ can be iterated across the loop in Fig. 1(a) until either goes to infinity, or it

converges to a fixed point. The iterative solution does not require the linearity of the characteristic $c(\cdot)$. On the other hand it is more restrictive than the analytic, as $y[n]$ converges only if $|b_0| < 1$ and, in the limit, when $b_0 = 1$ if $u[n] + q[n] = 0$. More in general, fixed point solvers rely on a contractive property of the network. This property, if holding, provides sufficient conditions for their convergence. In Wave Digital Networks the limit of having no more than one nonlinearity has been overcome by relaxing the port adaptation constraint, and then finding a fixed-point solution of the DFLs arising in the network thanks to their contractive behavior, descending from passivity of the network elements [33], [34]. The contractive hypothesis has also allowed for computing large Wave Digital Networks efficiently, using a relaxation method [35].

This intuition will be developed in the rest of the paper. In particular, it will be shown that if the network satisfies a contractive property, then its internal signals can be computed at every temporal step by means of a fixed-point search. The development will be regularly instantiated to the VCF aboard the EMS VCS3 synthesizer, a case study for which an *ad-hoc* fixed-point solution has already been computed [37]. Here, the filter model will be generalized in the length of the diode ladder shown in Fig. 2, similarly to what has been done for the Moog VCF [36].

The paper has the following structure: Sec. II provides a scalar algebraic form for characterizing linear DFL networks after their reformulation in terms of directed weighted graphs; Sec. III elaborates on such networks solution, particularly on its computation through fixed-point iteration; Sec. IV investigates the existence of a fixed-point solution and its relationship with the response of a "causal equivalent" of the DFL network; Sec. V extends the previous investigation to the nonlinear case, showing that a global fixed point exists if the DFL network satisfies a contractive property; Sec. VI discusses merits and limits of the proposed method, also in the light of research in circuit models where contraction is not needed; Sec. VII shows its application to a discrete-time model of the ring modulator. Finally, Sec. VIII concludes the paper.

II. Scalar DFL Networks: Algebraic Form

Without loss of generality, we restrict the formalization to DFL filter networks containing branches neither in parallel nor in series with each other inside one loop: the parallel can be replaced by a single branch summing the transfer characteristics; the series can be replaced by a single branch applying the transfer characteristics one after the other.

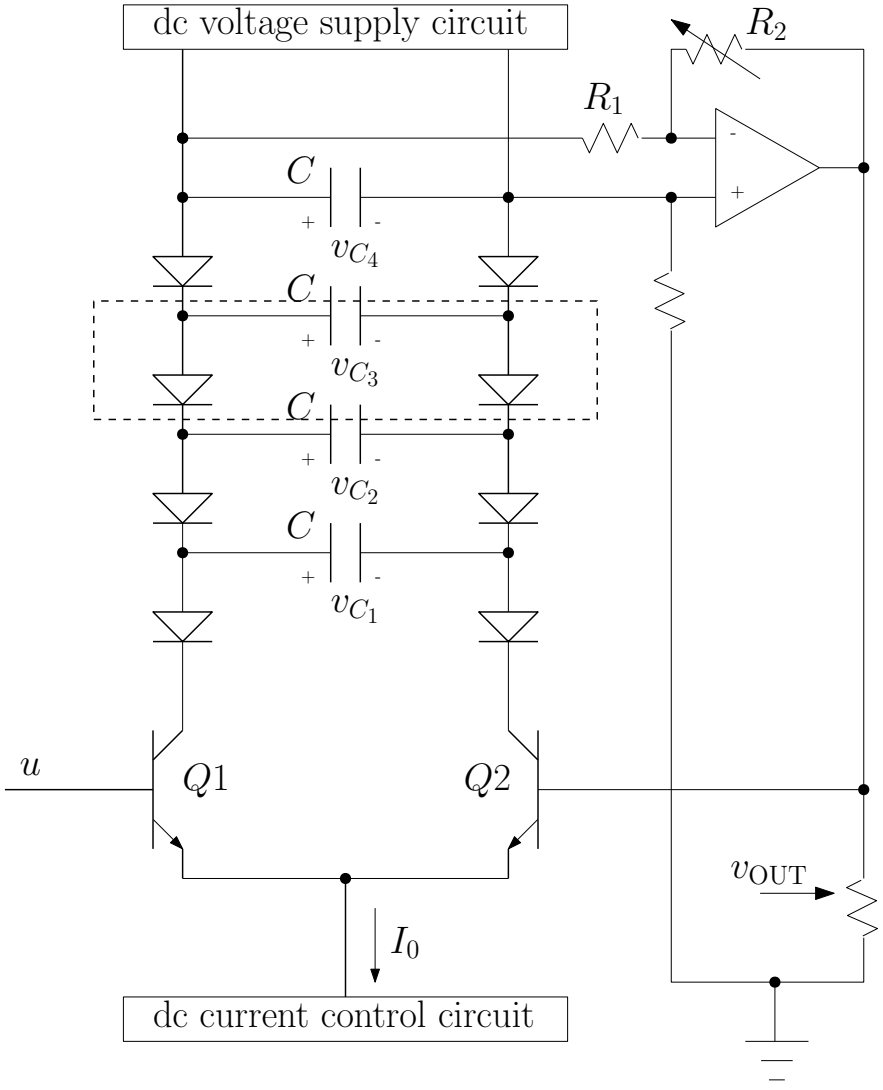

Fig. 2. EMS VCS3 voltage-controlled filter: particular of the small-signals circuit. One diode ladder element is surrounded by the rectangle in dashed line.

It will be convenient to start from the linear case. In this case we can put every DFL in the same form as in Fig. 1(c), and aggregate the contribution $q[n]$ depending on past input samples directly into the input $x[n] = u[n] + q[n]$ of a simpler DFL. After aggregation, the problem is reduced to solving a *scalar* DFL network [7].

We represent this network by means of a directed weighted graph, whose nodes correspond to the summation symbols appearing in the network. These nodes sum up the incoming signals at each temporal step similar to what happens in the network, for this reason we denote them with the same symbol. Bifurcations are conversely not represented in the graph, hence each node can

have several outgoing branches all carrying out the sum of the incoming signals.

Fig. 3 (right) represents the graph of the VCS3 VCF, whose DFL network [37] is reported in Fig. 3 (left) for convenience. This network results by performing a small-signals analysis of the EMS VCS3 circuitry, which finally leads to the following system of equations [37], [26], [32]:

$$\begin{cases} \dot{v}_{C_1} = \dfrac{I_0}{2C}\left(\tanh\dfrac{u - v_{\mathrm{OUT}}}{2V_T} + \tanh\dfrac{v_{C_2} - v_{C_1}}{2\sigma}\right) \\ \dot{v}_{C_2} = \dfrac{I_0}{2C}\left(\tanh\dfrac{v_{C_3} - v_{C_2}}{2\sigma} - \tanh\dfrac{v_{C_2} - v_{C_1}}{2\sigma}\right) \\ \dot{v}_{C_3} = \dfrac{I_0}{2C}\left(\tanh\dfrac{v_{C_4} - v_{C_3}}{2\sigma} - \tanh\dfrac{v_{C_3} - v_{C_2}}{2\sigma}\right) \\ \dot{v}_{C_4} = \dfrac{I_0}{2C}\left(-\tanh\dfrac{v_{C_4}}{6\sigma} - \tanh\dfrac{v_{C_4} - v_{C_3}}{2\sigma}\right) \\ v_{OUT} = \dfrac{2R_2 + R_1}{2R_1}\, v_{C_4} = \big(K + 1/2\big)\, v_{C_4} \end{cases} . \tag{2}$$

Such equations in their turn generate the DFL network. All parameters are present in the circuit in Fig. 2, except for σ and V_T that depend on the diode characteristic. Accessible controls in that circuit include the current I_0, driving the filter resonance frequency, and the factor $K = R_2/R_1$ responsible for the feedback and consequent resonance level. The reader is forwarded to [37] for a detailed development leading to the system (2).

In the linear case the blocks in Fig. 3 are approximated as $s(x) = sx$, $t(x) = tx$ and $r(x) = rx$, so that every branch simply rescales the signal coming from a node while sending it to another; in particular, the application in series of $s(\cdot)$ and $t(\cdot)$ linking node 8 to node 1 reduces to weighing the signal by the product of the respective coefficients. The same result is implied by the loopback on node 8, involving the application in series of $s(\cdot)$ and $r(\cdot)$.

A graph having N nodes can be expressed by means of a matrix $\boldsymbol{A}$ sized $N \times N$, such that $\boldsymbol{A}_{i,j} = \alpha$ if there is a branch with weight α linking node j to node i. Note that $\boldsymbol{A}$ is the transpose of the adjacency matrix of the graph [38]. In our example, labeling the $N = 8$ nodes as in Fig. 3, and after substitution of the nonlinear characteristics $r(\cdot)$, $s(\cdot)$ and $t(\cdot)$ with corresponding scalar

weights r, s and t, then

$$\boldsymbol{A}_{\mathrm{VCF}} = \begin{bmatrix} 0 & 0 & 0 & 0 & 0 & 0 & 0 & -ts \\ r & 0 & r & 0 & 0 & 0 & 0 & 0 \\ 0 & -s & 0 & s & 0 & 0 & 0 & 0 \\ 0 & 0 & -r & 0 & r & 0 & 0 & 0 \\ 0 & 0 & 0 & -s & 0 & s & 0 & 0 \\ 0 & 0 & 0 & 0 & -r & 0 & r & 0 \\ 0 & 0 & 0 & 0 & 0 & -s & 0 & s \\ 0 & 0 & 0 & 0 & 0 & 0 & -r & -rs \end{bmatrix}.$$

The elements of $\boldsymbol{A}_{\mathrm{VCF}}$ are distributed around the diagonal, apart from one in top right position. In fact, the nodes in Fig. 3 have been enumerated in a way that every branch connects a node only with itself and its adjacent nodes. In general, if node i is linked only with nodes $i-1$, i and $i+1$ through its outgoing branches then $\boldsymbol{A}$ is tridiagonal. If adjacency is also circular, meaning that nodes N and 1 can be joined as well, then two further nonzero elements appear in the rightmost top and leftmost bottom corners of $\boldsymbol{A}$. Due to the presence of the feedback amplifier, the VCF model leads to a graph exposing one circular adjacency from node 8 to node 1.

Let $\boldsymbol{v}$ be a column vector, whose ith element contains the signal value at node i. The ith entry of the product $\boldsymbol{A}\boldsymbol{v}$ gives the signal value at the same node in terms of the signals at the nodes linked to it. In fact, $\sum_j \boldsymbol{A}_{i,j}\boldsymbol{v}_j$ sums the contributions to node i coming from all nodes in the graph, each with its own respective weight. In particular, the contribution of the jth node is weighed by $\boldsymbol{A}_{i,j}$.

Through this matrix representation we can completely describe the behavior of a scalar DFL network at step n. We in fact consider a column vector $\boldsymbol{x}$, whose ith element contains the input at node i coming from outside the network. Then, the signal $\boldsymbol{v}$ inside the corresponding graph obeys the equation

$$\boldsymbol{v}[n] = \boldsymbol{A}\boldsymbol{v}[n] + \boldsymbol{x}[n]. \tag{3}$$

III. Network Solution

Eq. (3) defines a linear system at every temporal step. We will get rid of the discrete-time variable n throughout the whole section, aiming at adding focus to the analysis of this system:

$$(\boldsymbol{I} - \boldsymbol{A})\boldsymbol{v} = \boldsymbol{x}. \tag{4}$$

If $\boldsymbol{I}-\boldsymbol{A}$ is nonsingular then $\boldsymbol{v}=(\boldsymbol{I}-\boldsymbol{A})^{-1}\boldsymbol{x}$, meaning that the signal circulating in the network at step n depends entirely on external contributions at the same step—remember that $\boldsymbol{x}=\boldsymbol{u}+\boldsymbol{q}$, i.e., $\boldsymbol{x}$ accounts also for the filters' memory when the DFL network is linear.

We denote $\rho(\boldsymbol{A})$ to be the spectral radius of $\boldsymbol{A}$, that is, the magnitude of its largest eigenvalue. Now,

- if $\rho(\boldsymbol{A})<1$ then an iteration of the form

$$\boldsymbol{v}_{[k+1]}=\boldsymbol{A}\boldsymbol{v}_{[k]}+\boldsymbol{x} \tag{5}$$

  converges to $\boldsymbol{v}$ for an arbitrary choice of $\boldsymbol{v}_{[0]}$, the initial set of signal values at the nodes at step n. In this case Eq. (4) can be solved numerically through the fixed-point search (5), by iterating until k is such that $|\boldsymbol{v}_{[k+1]}-\boldsymbol{v}_{[k]}|$ fits below a desired precision threshold [39];
- if $\rho(\boldsymbol{A})\geq 1$ then the iteration is not guaranteed to converge, even if $\boldsymbol{I}-\boldsymbol{A}$ is not singular. As an example, let $\boldsymbol{A}=\begin{bmatrix}2 & 0\\ 0 & 0\end{bmatrix}$, so that $\rho(A)=2>1$. Clearly $\boldsymbol{I}-\boldsymbol{A}=\begin{bmatrix}-1 & 0\\ 0 & 1\end{bmatrix}$ is not singular. If $\boldsymbol{x}=\begin{bmatrix}1 & 0\end{bmatrix}^T$ then the vector $\boldsymbol{v}=\begin{bmatrix}-1 & 0\end{bmatrix}^T$ solves (4). However, if $\boldsymbol{v}_0=\begin{bmatrix}a & b\end{bmatrix}^T$ with $a\neq -1$ then the iteration (5) diverges.

The VCF network can be generalized [36], by cascading the element inside the rectangle in dashed line in Fig. 3 (left). This generalization follows by varying the extension of the diode ladder in Fig. 2. Fig. 4 illustrates effects of this variation if I_0 sets the VCF center frequency to 400 Hz, and K is set to 4 thus providing moderate resonance level around the same frequency in the canonical four-element ladder circuit. Increasing the number of elements causes the filter to become progressively more resonant, until entraining the circuit into self-oscillation. Note, however, that this oscillation saturates the filter with no explosion of the output. Similarly, progressively larger voltages as the magnitude-increasing impulses producing each output in Fig. 4 eventually saturate the filter, with no explosion of the output signal.

The consequent generalized graph of N nodes gives account of a cascade of $N/2$ such elements, producing an equally long motif inside the rectangle in dashed line in Fig. 3 (right). For this network, $\det(\boldsymbol{A}_{\mathrm{VCF}})=(ts)r(rs)^{N/2-1}=(rs)^{N/2}t$.

Since the determinant of a matrix is equal to the product of its N eigenvalues $\lambda_1,\ldots,\lambda_N$, i.e., $\det(\boldsymbol{A})=\prod_{i=1}^{N}\lambda_i$, then we can already conclude that if $|\det(\boldsymbol{A})|>1$ then $\rho(\boldsymbol{A})>1$. In this case it makes no sense to start an iterative fixed-point search. In our example this condition reduces to check whether

$$|rs|^{N/2}|t|>1 \quad \text{or} \quad |rs|>|t|^{-N/2}\ . \tag{6}$$

A critical parametric setting of the VCS3 VCF discrete-time model scales the signals by about $r = 1$, $s = 1500/F_s$ and $t = 10$, where F_s is the sampling rate of the simulation [37]. This setting reproduces a situation in which the voltage driving the resonance frequency and the feedback gain are both set to maximum. Using these parameters with $N = 8$ leads to $|rs|^{N/2}|t| \approx 10^{-5}$ if the model runs at $F_s = 44.1$ kHz. In the light of inequality (6), this result suggests possible and perhaps fast convergence of the fixed-point iteration especially for increasing values of N.

IV. Existence of the Numerical Solution

The eigenvalues of $\boldsymbol{A}$ are the roots of its characteristic polynomial $P_{\boldsymbol{A}}(\lambda) = \det(\lambda \boldsymbol{I} - \boldsymbol{A})$.

One further look to Eq. (5) shows that a fixed point is computed by repeatedly updating the signals at each node. Hence, the iterative procedure is implemented by constantly feeding the DFL network with the input value at step n until a fixed point is found out with sufficient precision. This procedure is equivalent to computing the response to dc (i.e., a constant signal) of a discrete-time filter network having the same topology, whose branches contain a delay unit in series with each coefficient. We call this derivation *causal equivalent* of the original DFL network.

It is straightforward to demonstrate that the causal equivalent is bounded-input bounded-output, shortly BIBO stable if and only if $\rho(\boldsymbol{A}) < 1$. In fact, by $\mathcal{Z}$-transforming (5) on the iteration index k we get

$$z\boldsymbol{V}(z) = \boldsymbol{A}\boldsymbol{V}(z) + \boldsymbol{X}(z), \tag{7}$$

in which $\boldsymbol{X}(z)$ is the $\mathcal{Z}$-transform of a constant extension of $\boldsymbol{x}$ along the iteration index. Moving $\boldsymbol{A}\boldsymbol{V}(z)$ to the left, and then multiplying both sides of the equation by $(z\boldsymbol{I} - \boldsymbol{A})^{-1}$ yields the transfer matrix of the causal equivalent:

$$\boldsymbol{V}(z) = (z\boldsymbol{I} - \boldsymbol{A})^{-1}\boldsymbol{X}(z) = \frac{\mathrm{adj}(z\boldsymbol{I} - \boldsymbol{A})}{\det(z\boldsymbol{I} - \boldsymbol{A})}\boldsymbol{X}(z), \tag{8}$$

in which the operator adj gives the adjoint matrix. Since $\det(z\boldsymbol{I} - \boldsymbol{A}) = P_{\boldsymbol{A}}(z)$ is the characteristic polynomial of $\boldsymbol{A}$ in z, the N poles $z_1, \ldots, z_N$ of the transfer matrix correspond to the eigenvalues of $\boldsymbol{A}$. Stability of the causal equivalent occurs if and only if $|z_i| < 1, i = 1, \ldots, N$, and this corresponds to have $\rho(\boldsymbol{A}) < 1$.

Computing the roots of $P_{\boldsymbol{A}}(\lambda)$ is often problematic, and other analysis tools can be used instead to figure out their positions in the complex plane. The Gershgorin theorem shows that

the N eigenvalues of $\boldsymbol{A}$ are contained inside the disks $\delta_i = \delta(\eta_i, \rho_i), i = 1, \ldots, N$, each defined to have center in $\eta_i = \boldsymbol{A}_{i,i}$ and radius

$$\rho_i = \sum_{\substack{j=1 \\ j \neq i}}^{N} |\boldsymbol{A}_{i,j}| \tag{9}$$

in the complex plane [40]. In our example, if the disks contain the eigenvalues of $\boldsymbol{A}_{\mathrm{VCF}}$ then they must contain also the (identical) eigenvalues of the similar matrix $\tilde{\boldsymbol{A}}_{\mathrm{VCF}} = \boldsymbol{D}(\alpha)\boldsymbol{A}_{\mathrm{VCF}}\boldsymbol{D}^{-1}(\alpha)$, with

$$\boldsymbol{D}(\alpha) = \begin{bmatrix} 1 & 0 & 0 & 0 & 0 & 0 & 0 & 0 \\ 0 & \alpha & 0 & 0 & 0 & 0 & 0 & 0 \\ 0 & 0 & 1 & 0 & 0 & 0 & 0 & 0 \\ 0 & 0 & 0 & \alpha & 0 & 0 & 0 & 0 \\ 0 & 0 & 0 & 0 & 1 & 0 & 0 & 0 \\ 0 & 0 & 0 & 0 & 0 & \alpha & 0 & 0 \\ 0 & 0 & 0 & 0 & 0 & 0 & 1 & 0 \\ 0 & 0 & 0 & 0 & 0 & 0 & 0 & \alpha \end{bmatrix}.$$

This endomorphism maps the coefficients r, s, and t respectively in $\tilde{r} = \alpha r$, $\tilde{s} = \alpha^{-1}s$, and $\tilde{t} = t$ in $\tilde{\boldsymbol{A}}_{\mathrm{VCF}}$. If applied to the similar matrix, the Gershgorin theorem provides N disks that reduce to four after pruning those having identical center and radius:

$$\begin{aligned} \delta_1 &= \delta(0, |t\alpha^{-1}s|), \quad \delta_2 = \delta(0, 2|\alpha r|) \\ \delta_3 &= \delta(0, 2|\alpha^{-1}s|), \quad \delta_4 = \delta(-rs, |\alpha r|) \end{aligned}. \tag{10}$$

Convergence to a fixed-point is guaranteed if their union is in the disk $\delta_\gamma = \delta(0, \gamma)$, with $\gamma < 1$. Disk δ_2 satisfies inclusion in δ_γ if $|\alpha| < \gamma(2|r|)^{-1}$. Importing this inequality while minimizing $|s|$ between radii ρ_1 and ρ_3 offers:

$$|s| \leq \min\Big\{\gamma\frac{|\alpha|}{2}, \gamma\frac{|\alpha|}{|t|}\Big\} \leq \min\Big\{\frac{\gamma^2}{4|r|}, \frac{\gamma^2}{2|rt|}\Big\}. \tag{11}$$

This condition, along with the previous constraint on $|\alpha|$, guarantees that δ_4 is in δ_γ as well:

$$|rs| + |\alpha r| \leq \frac{\gamma^2}{4} + \frac{\gamma}{2} < \frac{3}{4}\gamma\,. \tag{12}$$

As opposed to the necessary condition (6) that we checked on the spectral radius by computing $\det(\boldsymbol{A}_{\mathrm{VCF}})$, the Gershgorin's disks establish no dependency on $N/2$, the length of the VCF ladder. Furthermore, the VCF model always satisfies $|r| \leq 1$. Since $|rt| \approx 10$ when the filter feedback gain is set to maximum, condition (11) requires $|s| \lessapprox 0.05$, a magnitude we have seen

this scaling parameter meets as soon as the sampling rate in the digital model is set to about 30 kHz or greater.

Condition (11) not only puts a sufficient constraint on the spectral radius. It also establishes an identical inequality for the following matrix norm:

$$\begin{aligned} \|\boldsymbol{A}\|_{\boldsymbol{D}(\alpha),\infty} &= \|\boldsymbol{D}(\alpha)\boldsymbol{A}\boldsymbol{D}^{-1}(\alpha)\|_\infty \\ &= \max_i \sum_{j=1}^{N} \left|\left(\boldsymbol{D}(\alpha)\boldsymbol{A}\boldsymbol{D}^{-1}(\alpha)\right)_{i,j}\right| . \end{aligned} \tag{13}$$

This norm [41] is induced by the vector norm $\|\boldsymbol{x}\|_{\boldsymbol{D}(\alpha),\infty} = \|\boldsymbol{D}(\alpha)\boldsymbol{x}\|_\infty = \max_i \left|\left(\boldsymbol{D}(\alpha)\boldsymbol{x}\right)_i\right|$. Specifically in our example, condition (11) implies

$$\|\boldsymbol{A}_{\mathrm{VCF}}\|_{\boldsymbol{D}(\alpha),\infty} < \gamma. \tag{14}$$

We will make use of this inequality in the next section, while dealing with the nonlinear case.

V. Existence of the Nonlinear Solution

We deal with nonlinear DFL networks by generalizing the coefficients in $\boldsymbol{A}$ into functions $f_{i,j} : \mathbb{R} \to \mathbb{R}$ of the corresponding scalar input $\boldsymbol{v}_j$. Hence, at every step the output from the nodes results by applying a function $f : \mathbb{R}^N \to \mathbb{R}^N$ whose components $f_1, \ldots, f_N$ are such that

$$f_i(\boldsymbol{v}) = \sum_{j=1}^{N} f_{i,j}(\boldsymbol{v}_j), \qquad i = 1, \ldots, N. \tag{15}$$

If the functions $f_{i,j}$ are derivable each with continuous derivative, then

$$\begin{aligned} f_i(\boldsymbol{u}) - f_i(\boldsymbol{v}) &= \sum_{j=1}^{N} f_{i,j}(\boldsymbol{u}_j) - f_{i,j}(\boldsymbol{v}_j) \\ &= \sum_{j=1}^{N} f'_{i,j}(\xi_{i,j})(\boldsymbol{u}_j - \boldsymbol{v}_j), \end{aligned} \tag{16}$$

with $\boldsymbol{u}_j \le \xi_{i,j} \le \boldsymbol{v}_j$. If we denote with $\boldsymbol{\Xi}$ the matrix whose entries are the values $\xi_{i,j}$ with $i, j \in 1, \ldots, N$, then

$$f(\boldsymbol{u}) - f(\boldsymbol{v}) = \boldsymbol{J}_f(\boldsymbol{\Xi})(\boldsymbol{u} - \boldsymbol{v}), \tag{17}$$

in which $\boldsymbol{J}_f(\boldsymbol{\Xi})$ is the matrix whose entries are the values $f'_{i,j}(\xi_{i,j})$.

For every vector norm and its induced matrix norm the following inequality holds [41]:

$$\|f(\boldsymbol{u}) - f(\boldsymbol{v})\| \le \|\boldsymbol{J}_f(\boldsymbol{\Xi})\|\|(\boldsymbol{u} - \boldsymbol{v})\|. \tag{18}$$

If $\|\boldsymbol{J}_f(\boldsymbol{\Xi})\| \leq \gamma < 1 \ \ \forall \boldsymbol{\Xi} \in \mathbb{R}^{N\times N}$, then f is a *contraction* over $\mathbb{R}^N$. This condition is strong enough to guarantee that the equation $\boldsymbol{v} = f(\boldsymbol{v}) + \boldsymbol{x}$ has a unique fixed point that can be searched through the iteration $\boldsymbol{v}_{[k+1]} = f(\boldsymbol{v}_{[k]}) + \boldsymbol{x}$ [42]. Such two formulas respectively generalize (3) and (5) to the nonlinear case.

In the case of the VCF, $\boldsymbol{J}_f$ is obtained starting from $\boldsymbol{A}_{\mathrm{VCF}}$ by assuming $r(x) = \tanh(x/\chi)$, $s(x) = sx$, and $t(x) = tx$. Later in this section χ will be properly set among three possible values: $2V_T$, 2σ and 6σ, all appearing as arguments of the $\tanh$ functions in (2). The consequent matrix, we call it $\boldsymbol{J}_{\mathrm{VCF}}$, hence is equal to (19) with $r'(\xi_{i,j}) = (1/\chi)\{1 - \tanh^2(\xi_{i,j}/\chi)\}$, $s'(\xi_{i,j}) = s$ and $t'(\xi_{i,j}) = t$.

Let $\|f\|_\infty = \sup_{x\in\mathbb{R}} |f(x)|$. Similarly to what we figured out in Sec. IV when applying the Gershgorin theorem to $\boldsymbol{A}_{\mathrm{VCF}}$, if $\|r'\|_\infty$ is limited then we can rewrite (11):

$$\|r'\|_\infty \leq \min\Big\{\frac{\gamma^2}{4\|s'\|_\infty}, \frac{\gamma^2}{2\|s'\|_\infty\|t'\|_\infty}\Big\} = \frac{\gamma^2}{2|st|}, \tag{20}$$

where the last term follows when t is set to be critical. Holding this condition then $\|\boldsymbol{J}_{\mathrm{VCF}}(\boldsymbol{\Xi})\|_{\boldsymbol{D}(\alpha),\infty} < \gamma$ and this, if $\gamma < 1$ in its turn, guarantees the convergence of the iteration $\boldsymbol{v}_{[k+1]} = f(\boldsymbol{v}_{[k]}) + \boldsymbol{x}$ with a speed that eventually will be inversely proportional to γ. In fact, the smaller the radius γ, the faster the convergence is [39].

Condition (20) predicts the behavior of the VCF model simulations better than the linear estimate (11). Holding

$$\|r'\|_\infty = \frac{1}{\chi}\Big\|1 - \tanh^2(\frac{x}{\chi})\Big\|_\infty = \frac{1}{\chi} \leq \frac{1}{0.052}, \tag{21}$$

where we have selected the smallest (i.e., worst-case) voltage parameter $\chi = 2V_T = 0.052$ in the model [37], (20) suggests that small values of $|s|$ and $|t|$ afford faster convergence to the fixed point thanks to the possibility for γ to be small, too. Conversely, an increase of $|s|$—consequence of shifting upward the resonance frequency of the filter by rising the characteristic point of the diodes forming the ladder—rapidly slows down the convergence, because γ is pushed toward the unit boundary by a quadratic law. If we recall the worst-case parameterization given in Sec. III, (20) and (21) immediately yield

$$\frac{1}{0.052} \leq \min\Big\{\frac{\gamma^2 F_s}{6\cdot 10^3}, \frac{\gamma^2 F_s}{3\cdot 10^4}\Big\}, \text{ thus } \gamma \gtrapprox \sqrt{\frac{577\cdot 10^3}{F_s}},$$

meaning in practice that convergence of the fixed-point iteration is guaranteed for every choice of the filter parameters if the model is sampled at a rate of 577 kHz, or greater.

This conclusion matches well with previous simulations of the VCS3 VCF digital model, whose real-time implementation at 48 kHz was particularly efficient unless the resonance frequency was turned up above few thousand Hertz in presence of moderate or strong feedback gain: with this choice of the parameters, the number of fixed-point iterations hit the upper bound protecting the system from excessive computational load [37].

VI. Discussion

The proposed method can be applied to a discrete-time filter network model containing one or more DFL. Holding contractive property (18), at every temporal step it refines the solution by finding out—with increasing precision with the number of iterates—values that accommodate the instantaneous dependencies existing among the blocks in the network. The method operates irrespective of the discretization technique, hence it is applicable in general whenever a DFL appears in the digital network resulting after discretization.

In its current state the method cannot handle nonlinear combinations of the variables, including simple geometric nonlinearities of the type $f_k(\boldsymbol{v}) = \boldsymbol{v}_i \boldsymbol{v}_j$ with $i \neq j$ for some k. This limitation corresponds to having network graphs containing only summation nodes. It descends from (15), defining $f_i(\boldsymbol{v})$ as a superposition of (either linear or not) scalar terms $f_{i,1}(\boldsymbol{v}_1), \ldots, f_{i,N}(\boldsymbol{v}_N)$. Such a definition implies in particular that the method cannot deal with most situations in which an *internal* signal is used for instantaneous dynamic control. An intractable DFL of this type would arise in the VCF model, if the output from the filter was short-circuited back to the system through the resonance frequency control input. An extension of the method to network blocks accepting multiple signal variables requires a generalization of Eqs. (15)–(18), a possible object of future research.

Conversely, dynamic changes of the VCS3 VCF parameters s and t driven by *external* voltage signals—for instance sinusoids, often adopted by musicians to control the resonance point and, less frequently, the feedback gain—result in constant derivatives. There is in fact no dependency on $\boldsymbol{v}$ in such voltage functions. In other words, at every temporal step s' and t' simply "freeze" to the respective value s and t they are equal to in that moment: at this point they are subjected to condition (20), hence required to stay in the parametric ranges we have already seen in Sec. III.

Fixed-point solvers are known for their low speed of convergence. Recent results in musical circuit modeling successfully investigated alternative solutions, leading to nonlinear Wave Digital Networks whose DFL blocks have been computed using Newton's methods [43] or the K-method

[15], solving a nonlinear Wave Digital DFL through table lookup [44]. In both cases the contractive property became unnecessary. Particularly in the case of the VCS3 VCF, whose discrete-time model was obtained by bilinear transformation of the analog blocks, the computational issues we mentioned at the end of Sec. V were eventually overcome through a polynomial rearrangement of the nonlinear equations, exploiting the self-similarity of the derivative of the hyperbolic tangent. This rearrangement resulted in a digital realization converging in six iterations or less at 176 kHz, irrespectively of the parametric settings [45].

The possibility to include more efficient solvers in our method, and the structural changes this inclusion would determine in the original network structure are left to future research. For the moment, the proposed method can be used as a prototyping tool that furthermore unveils critical ranges of the driving parameters.

Sometimes, virtual analogue system designers have guaranteed explicit computability of their filter network realizations by inserting at least one fictitious unit delay. Perhaps counterintuitively, the stability of such a network does *not* imply convergence of the fixed-point solution in the original DFL realization under identical input and parameter values. In principle the network including fictitious delays is merely a modified version of the DFL network, whose causal equivalent might be unstable under certain conditions as opposed to its reformulation containing additional delays. This situation happens in systems whose norm $\|\boldsymbol{J}_f(\boldsymbol{\Xi})\|$ dramatically increases at certain temporal steps in consequence of the abrupt change in the values of some scalar derivatives $f_{i,j}$, abolishing the contractive property of f. The VCS3 VCF model is exempt from the risk of unexpected instability, since (20) depends only on external parameters. An example where conversely this situation can happen is reported in the next section.

VII. Example: Ring Modulator

As an application example we have chosen the ring modulator circuit shown in Fig. 5 (above). Thanks to the closed-loop connection of four diodes, the circuit generates an output voltage $v_{\text{OUT}}(t)$ by multiplying (in an analogue sense) two inputs $m(t)$ and $c(t)$, respectively a modulator and a carrier signal. Its model description in Fig. 5 (below) was obtained by loading the output point with a resistance R_a, and then by putting the carrier source resistance R_i in parallel with a regularizing capacitance C_p [46]. This analogue model leads to a system of two current and seven voltage ordinary differential equations establishing the filter network in Fig. 6, in which the voltages v_1, v_2 at the transformers and v_3 in series with the carrier signal are fed back to

the blocks computing the currents i_1, i_2 at the transformers and the voltages v_4, v_5, v_6, v_7 at the diodes. In this network, $C = C_p = 10^{-9}$ F, $L = 0.8$ H, $R_a = 600\ \Omega$, $R_i = 50\ \Omega$, $R_m = 80\ \Omega$, and $g(v) = 0.17v^4$ approximates the 1N270 germanium diode voltage-to-current characteristic at low positive voltages, with $g(v) = 0$ if $v < 0$ [46]. Finally, v_2 is also the output voltage.

Each differential block in Fig. 6 can be discretized with explicit or implicit methods. The former compute the output using past values of the input. The latter compute the output at step n once the input at the same step is known, in general being more accurate and stable meanwhile giving rise to the DFL problem if used everywhere in the network. Real-time digital audio effects often trade off between efficiency and accuracy, by realizing a discrete-time model avoiding the DFL problem meanwhile computing the differential blocks with implicit methods wherever possible. If Euler methods are used, then backward ($v[n] = v[n-1] + x[n]/F_s$, implicit) differs from forward ($v[n] = v[n-1] + x[n-1]/F_s$, explicit) Euler by the presence of an equivalent unit, delaying the input by $1/F_s$ s.

In the case of the ring modulator such a trade-off can be realized by discretizing the feed-forward blocks with forward Euler, and the feedback blocks with backward Euler. We will refer to this realization as "explicit solver" [46]. On the other hand, the fixed-point iteration can be used for comparing DFL network realizations based on different discretization methods. In our application example the explicit solver will be compared against two implicit realizations of the network, respectively computing each block with backward Euler or with trapezoidal rule, i.e. $v[n] = v[n-1] + (x[n] + x[n-1])/(2F_s)$.

Both realizations are described by the difference equation system (22) depending on how the

parameter μ is set: $\mu = 1$ for backward Euler, or $\mu = 1/2$ for trapezoidal rule.

$$
\begin{aligned}
v_1 =& \frac{\mu R_m}{\mu + CF_sR_m}\Big(\frac{m}{R_m} + i_1 - \\
& - \frac{g(v_4)}{2} + \frac{g(v_5)}{2} - \frac{g(v_6)}{2} + \frac{g(v_7)}{2}\Big) + \mathrm{past}_{v_1} \\
v_2 =& \frac{\mu R_a}{\mu + CF_sR_a}\Big(i_2 + \\
& + \frac{g(v_4)}{2} - \frac{g(v_5)}{2} - \frac{g(v_6)}{2} + \frac{g(v_7)}{2}\Big) + \mathrm{past}_{v_2} \\
v_3 =& \frac{\mu R_i}{\mu + C_pF_sR_i}\Big(g(v_4) + g(v_5) - g(v_6) - g(v_7)\Big) + \mathrm{past}_{v_3} \\
v_4 =& \frac{v_1}{2} - \frac{v_2}{2} - v_3 - c \\
v_5 =& -\frac{v_1}{2} + \frac{v_2}{2} - v_3 - c \\
v_6 =& \frac{v_1}{2} + \frac{v_2}{2} + v_3 + c \\
v_7 =& -\frac{v_1}{2} - \frac{v_2}{2} + v_3 + c \\
i_1 =& -\frac{\mu}{LF_s}v_1 + \mathrm{past}_{i_1} \\
i_2 =& -\frac{\mu}{LF_s}v_2 + \mathrm{past}_{i_2}.
\end{aligned}
\tag{22}
$$

In the above system the terms in $n-1$ have been conglomerated within the term past. Such terms are unimportant for the study of convergence and can be straightforwardly figured out, by respectively applying backward Euler or the trapezoidal rule to the differential equation system described by the filter network in Fig. 6.

The delay-free network is described by the graph in Fig. 7. The matrix $\boldsymbol{J}_{\mathrm{RM}}$ (23) of the derivatives obtained from (22) follows accordingly, in which

$$\rho_m = \frac{\mu R_m}{\mu + CF_sR_m},\ \rho_a = \frac{\mu R_a}{\mu + CF_sR_a},\ \rho_i = \frac{\mu R_i}{\mu + C_pF_sR_i}.$$

This time we set up an endomorphism by making use of a matrix $\boldsymbol{D}(\alpha, \beta)$ which is defined as

follows:

$$\boldsymbol{D}(\alpha,\beta)=\begin{bmatrix}\alpha&0&0&0&0&0&0&0&0\\0&\alpha&0&0&0&0&0&0&0\\0&0&\alpha&0&0&0&0&0&0\\0&0&0&1&0&0&0&0&0\\0&0&0&0&1&0&0&0&0\\0&0&0&0&0&1&0&0&0\\0&0&0&0&0&0&1&0&0\\0&0&0&0&0&0&0&\beta&0\\0&0&0&0&0&0&0&0&\beta\end{bmatrix}.$$

An inequality equivalent to (20) can be found by choosing $\alpha = 2/\gamma$. This choice guarantees that the constant entries appearing in the six lower rows of $\boldsymbol{D}(\alpha,\beta)\boldsymbol{J}_{\mathrm{RM}}\boldsymbol{D}^{-1}(\alpha,\beta)$ sum up in magnitude exactly to γ. Now, the last two rows determine a Gershgorin disk providing the condition $\beta\alpha^{-1}\mu/(LF_s) \leq \gamma$, that gives $\beta \leq 2LF_s/\mu = 1.6F_s/\mu$. In parallel the first row gives the inequality $\rho_m\beta^{-1}\alpha + 2\|g'\|_\infty\rho_m\alpha < \gamma$, equivalent to

$$\|g'\|_\infty \leq \frac{\gamma^2}{4\rho_m} - \frac{1}{2\beta} = \frac{\gamma^2}{4}\Big(\frac{1}{R_m} + \frac{CF_s}{\mu}\Big) - \frac{1}{2\beta}. \tag{24}$$

Analogously, the second row gives

$$\|g'\|_\infty \leq \frac{\gamma^2}{4\rho_a} - \frac{1}{2\beta} = \frac{\gamma^2}{4}\Big(\frac{1}{R_a} + \frac{CF_s}{\mu}\Big) - \frac{1}{2\beta}, \tag{25}$$

and since $R_a > R_m$, inequality (25) is stronger than (24). Finally, the third row gives

$$\|g'\|_\infty \leq \frac{\gamma^2}{8\rho_i} = \frac{\gamma^2}{8}\Big(\frac{1}{R_i} + \frac{C_pF_s}{\mu}\Big). \tag{26}$$

A formal stability analysis is probably of no primary interest while prototyping different implicit solvers of the network in Fig. 6 using the fixed-point method, however it suggests interesting conclusions once the circuit parameters are looked again. Inequalities (24) and (25) are initially bound by the negative term $-1/(2\beta) \leq -\mu/(3.2F_s)$, meaning that no convergence to the fixed point is possible unless F_s is turned up until the positive term $\gamma^2/(4R_a) = \gamma^2/2400$ counterbalances $-1/(2\beta)$. Choosing for instance to solve with backward Euler, i.e. $\mu = 1$, in the limit $1/(2\beta) = \mu/(3.2F_s)$ and $\gamma = 1$ this happens if

$$\frac{1}{3.2F_s} \leq \frac{1}{2400}, \text{ thus } F_s \geq 750 \text{ Hz}. \tag{27}$$

From this sampling frequency value, all inequalities remain essentially unchanged until the term $CF_s/\mu = C_pF_s/\mu$ starts to dominate over $1/R_i$ proportionally with F_s. This, however, happens when the sampling frequency is turned up until some hundred kHz.

As opposed to the VCS3 VCF, whose fixed-point convergence is signal-independent, larger voltage amplitudes in the ring modulator circuit rapidly increase the derivative g' of the currents flowing through the diodes, pushing the fixed-point search toward instability unless F_s is further increased. It must be also noticed that at high sampling rates the bound (26) depends on the product $\gamma^2 C_p F_s$. This means that faster convergence afforded by smaller γ values results in smaller ranges of convergence as a side effect. In practice we expect that higher sampling rates may accelerate the convergence, however with no proportional benefit in terms of stability. This conclusion suggests a problematic fixed-point solution of the digital ring modulator model, as we should ultimately expect in front of four 4th-order polynomial nonlinearities operating in the circuit.

A. Simulations

The explicit solver has been compared against the DFL realizations obtained through backward Euler and trapezoidal rule in three conditions, each considering two input sine waves having a common amplitude but different frequencies respectively for the modulator and carrier signal: 150 mV, 500 Hz and 100 Hz for simulation 1; 150 mV, 5 kHz and 500 Hz for simulation 2; 500 mV, 5 kHz and 500 Hz for simulation 3. In all such conditions the carrier was first constantly set to 100 mV for 3 ms—see Fig. 8 (above). The fixed-point solution was approximated by stopping the search when $|\boldsymbol{v}_{2,[k+1]} - \boldsymbol{v}_{2,[k]}| < 10^{-4}$, i.e., when the magnitude error affecting the output signal was less than 0.1 mV. In all simulations a reference sampling rate $F_s = 44.1$ kHz was oversampled by a factor l, which was empirically set to be the smallest factor guaranteeing stability of the simulation running on a Linux Octave software environment. Fig. 8 (below) shows the output of simulation 2 during the first 10 ms using backward Euler, while Fig. 9 shows the corresponding spectrum up to the Nyquist frequency, limited to when the carrier was sinusoidal along 200 ms.

Table I summarizes the results, all referring to simulations lasting 0.5 s. For each simulation, the table shows the computations a solver on average made to produce an output sample. Figures of computation result by multiplying l times the average number of iterations the solver made along the simulation—see Fig. 10. The explicit solver obviously did not need to iterate.

TABLE I

AVERAGE NUMBER OF COMPUTATIONS FOR DIFFERENT SIMULATION METHODS AT EVERY TEMPORAL STEP

Solver	Simulation 1	Simulation 2	Simulation 3
explicit	28	27	65
backwd E.	$23 \cdot 1.9 = 43.7$	$22 \cdot 2.8 = 61.6$	$99 \cdot 3.6 = 356.4$
trapezoidal	$29 \cdot 1.1 = 31.9$	$29 \cdot 2.1 = 60.9$	$71 \cdot 4.9 = 347.9$

All methods show low sensitivity to the frequency of the modulator and carrier sine waves. Conversely, if their amplitude is increased to 500 mV, a value which pushes the diodes to an almost identical operating voltage, then the oversampling factor must be increased. Especially backward Euler needs this factor to be substantially turned up. However, once in the stability range this solver does not computationally cost much more than the trapezoidal rule, as the fixed-point solution requires proportionally less iterations on average.

The explicit solver is more efficient than the implicit procedures, particularly during simulation 3. Relaxing the stop condition shifts backward Euler toward the performance of the explicit solver, i.e., less iterations at the cost of proportionally higher oversampling factors. In parallel the trapezoidal rule is less flexible, although it still benefits in term of computations from a relaxation of the stop condition.

The higher cost of the implicit procedures is probably rewarded in terms of accuracy of the output. This conclusion is supported by comparing, during simulation 2, the explicit solution obtained using forward Euler against the implicit solution obtained using backward Euler. Even if stability holds for both solvers, Fig. 11 shows that an appreciable difference exists between the two solutions. In particular, this difference becomes temporarily comparable to the output signal magnitudes immediately after the carrier signal has switched from constant to sinusoidal. Since, by observing Fig. 10, this transient comes together with slower convergence—remember the fixed-point solver checks an absolute threshold value at every iteration—we conclude that the implicit solution during this transient defines a trajectory which is closer to the output of the analog model.

The simulations of the ring modulator reinforce the idea that the fixed-point solution of a DFL network brings benefit especially during the prototyping stage, when the behavior and accuracy of different block discretizations should be checked in relatively little time. Based on

such prototypes, more advanced solvers can be evaluated and eventually realized. To this regard, nonlinear Wave Digital Networks such as those mentioned in Secs. I and VI offer an attractive alternative also because recently they have modeled systems that are not strictly passive. In this case, non-contraction has been efficiently worked around using Newton's solvers [43]. These networks, hence, now may handle characteristics such as the polynomial diode approximation $g(\cdot)$ proposed for our ring modulator model. In fact, literature published when this manuscript was under revision has solved the same ring modulator circuit efficiently by means of a hybrid Wave Digital model, whose diode function was set to admit little reverse current to favor stability [47]. The nonlinear DFLs arising in that wave-based hybrid model were computed using a Newton method.

VIII. Conclusion

A method for the explicit computation of nonlinear filter networks containing DFLs has been presented. In presence of a contractive property, such networks allow for a fixed-point search of the signals flowing along the loops. In spite of its flexibility and immediacy of application, inherent numerical issues affecting fixed-point schemes limit the power and effectiveness of the proposed method. On the other hand a fixed-point search can become useful during the digital model prototyping stage, provided also the possibility to figure out the range of frequency rates in which fixed-point convergence is guaranteed once a numerical solver has been selected for the filter blocks. Such features have been tested on a ring modulator model, whose realization in the discrete-time is complicated by the the closed-loop connection of four polynomial nonlinearities.

Although in the Kirchhoff domain, our method currently faces technical obstacles similar to those that have been recently dealt with by Wave Digital Networks, whose multiple nonlinearities require efficient methods to compute the DFLs [43], [44], [48]. Future research will aim at understanding if the substitution of the fixed-point with Newton iteration can still preserve the original network structure, as well as if the latter can allow for a convergence analysis similar to what the fixed-point solver made possible to do.

Acknowledgment

The authors thank the reviewers for their careful reading of the manuscript, and acknowledge the support of the PRID project ENCASE funded by the University of Udine.

REFERENCES

[1] J. Szczupak and S. K. Mitra, "Detection, location, and removal of delay-free loops in digital filter configurations," *IEEE Trans. on Acoustics, Speech and Signal Processing*, vol. 23, no. 6, pp. 558–562, 1975.

[2] A. Härmä, "Implementation of frequency-warped recursive filters," *EURASIP Signal Processing*, vol. 80, no. 3, pp. 543–548, Mar. 2000.

[3] W. Pirkle, "Resolving delay-free loops in recursive filters using the modified Härmä method," in *Audio Engineering Society Convention 137*. Audio Engineering Society, Los Angeles, United States, 9-12 Oct. 2014, pp. 720–729. Available: http://www.aes.org/e-lib/browse.cfm?elib=17517

[4] A. Härmä, M. Karjalainen, L. Savioja, V. Välimäki, U. K. Laine, and J. Huopaniemi, "Frequency-warped signal processing for audio applications," *J. of the Audio Engineering Society*, vol. 48, no. 11, pp. 1011–1031, Nov. 2000.

[5] F. Fontana and M. Karjalainen, "A digital bandpass/bandstop complementary equalization filter with independent tuning characteristics," *IEEE Signal Processing Letters*, vol. 10, no. 4, pp. 88–91, Apr. 2003.

[6] F. Fontana, "Preserving the structure of the Moog VCF in the digital domain," in *Proc. Int. Computer Music Conf.*, Copenhagen, Denmark, 27–31 Aug. 2007, pp. 291–294.

[7] ——, "Computation of linear filter networks containing delay-free loops, with an application to the waveguide mesh," *IEEE Trans. on Speech and Audio Processing*, vol. 11, no. 6, pp. 774–782, Nov. 2003.

[8] V. Zavalishin, "Preserving the LTI system topology in s-to z-plane transforms," Native Instruments, Tech. Rep., 2008.

[9] ——, "The art of VA filter design," Native Instruments, Tech. Rep., 2012.

[10] D. Berners and J. S. Abel, "Discrete-time implementation of arbitrary delay-free feedback networks," in *Audio Engineering Society Convention 141*, Los Angeles, United States, Sept. 2016. Available: http://www.aes.org/e-lib/browse.cfm?elib=18489

[11] F. Fontana and F. Avanzini, "Computation of delay-free nonlinear digital filter networks. Application to chaotic circuits and intracellular signal transduction," *IEEE Trans. on Signal Processing*, vol. 56, no. 10, pp. 4703–4715, Oct. 2008.

[12] F. Avanzini and F. Fontana, "Exact discrete-time realization of a Dolby B encoding/decoding architecture," in *Proc. Conf. on Digital Audio Effects (DAFX-06)*, Montreal, Quebec, Canada, Sept. 18–20, 2006, pp. 297–302.

[13] D. T. Yeh, J. S. Abel, and J. O. Smith, "Automated physical modeling of nonlinear audio circuits for real-time audio effects – Part I: Theoretical development," *IEEE Trans. on Audio, Speech and Language Processing*, vol. 18, no. 4, pp. 728–737, 2010.

[14] D. T. Yeh, "Automated physical modeling of nonlinear audio circuits for real-time audio effects – Part II: BJT and vacuum tube examples," *IEEE Trans. on Audio, Speech and Language Processing*, vol. 20, no. 4, pp. 1207–1216, May 2012.

[15] G. Borin, G. De Poli, and D. Rocchesso, "Elimination of delay-free loops in discrete-time models of nonlinear acoustic systems," *IEEE Trans. on Speech and Audio Processing*, vol. 8, no. 5, pp. 597–605, 2000.

[16] F. Avanzini and D. Rocchesso, "Modeling collision sounds: Non-linear contact force," in *Proc. Conf. on Digital Audio Effects (DAFX-01)*, Limerick, Ireland, Dec. 2001, pp. 61–66.

[17] B. Bank, S. Zambon, and F. Fontana, "A modal-based real-time piano synthesizer," *IEEE Trans. on Audio, Speech and Language Processing*, vol. 18, no. 4, pp. 809–821, 2010, special Issue on Virtual Analog Audio Effects and Musical Instruments.

[18] M. Karjalainen, C. Erkut, and L. Savioja, "Compilation of unified physical models for efficient sound synthesis," in *Proc. IEEE Int. Conf. on Acoustics, Speech, and Signal Processing (ICASSP '03)*, vol. 5, April 2003, pp. 433–436.

[19] A. Sarti and G. D. Sanctis, "Systematic methods for the implementation of nonlinear wave-digital structures," *IEEE Trans. on Circuits and Systems*, vol. 56, no. 2, pp. 460–472, Feb. 2009.

[20] K. J. Werner, J. O. Smith III, and J. S. Abel, "Wave digital filter adaptors for arbitrary topologies and multiport linear elements," in *Proc. Conf. on Digital Audio Effects (DAFX-15)*, Trondheim, Norway, Nov. 2015, pp. 379–386.

[21] M. Holters and U. Zölzer, "A generalized method for the derivation of non-linear state-space models from circuit schematics," in *23rd European Signal Processing Conference (EUSIPCO)*, Nice, France, Aug. 2015, pp. 1073–1077.

[22] ——, "A k-d tree based solution cache for the non-linear equation of circuit simulations," in *24th European Signal Processing Conference (EUSIPCO)*, Budapest, Hungary, Aug. 2016, pp. 1028–1032.

[23] ——, "Automatic decomposition of non-linear equation systems in audio effect circuit simulation," in *Proc. Conf. on Digital Audio Effects (DAFX-17)*, Edinburgh, UK, Sept. 2017, pp. 138–144.

[24] L. Trautmann and R. Rabenstein, *Digital sound synthesis by physical modeling using the functional transformation method*. Berlin: Springer, 2012.

[25] A. Falaize and T. Hélie, "Passive guaranteed simulation of analog audio circuits: A port-Hamiltonian approach," *Applied Sciences*, vol. 6, no. 10, p. 273, 2016.

[26] S. D'Angelo and V. Välimäki, "Generalized Moog ladder filter: Part II – Explicit nonlinear model through a novel delay-free loop implementation method," *IEEE/ACM Trans. on Audio, Speech and Language Processing*, vol. 22, no. 12, pp. 1873–1883, Dec. 2014.

[27] A. Bernardini, K. J. Werner, A. Sarti, and J. O. Smith, "Modeling nonlinear wave digital elements using the Lambert function," *IEEE Transactions on Circuits and Systems I: Regular Papers*, vol. 63, no. 8, pp. 1231–1242, Aug. 2016.

[28] M. Holters and U. Zölzer, "Physical modelling of a wahwah effect pedal as a case study for application of the nodal DK method to circuits with variable parts," in *Proc. Digital Audio Effects (DAFx-11)*, Paris, France, 2011, pp. 31–35.

[29] J. Parker, "A simple digital model of the diode-based ring-modulator," in *Proc. Digital Audio Effects (DAFx-11)*, Paris, France, 2011, pp. 163–166.

[30] F. Eichas, M. Fink, M. Holters, and U. Zölzer, "Physical modeling of the MXR Phase 90 Guitar Effect Pedal," in *Proc. Digital Audio Effects (DAFx-14)*, Erlangen-Nürnberg, Germany, 2014, pp. 153–158.

[31] R. C. D. de Paiva, J. Pakarinen, V. Välimäki, and M. Tikander, "Real-time audio transformer emulation for virtual tube amplifiers," *EURASIP Journal on Advances in Signal Processing*, vol. 2011, p. 347645, 2011.

[32] F. Esqueda, H. Pöntynen, J. D. Parker, and S. Bilbao, "Virtual analog models of the Lockhart and Serge wavefolders," *Applied Sciences*, vol. 7, no. 12, 2017.

[33] T. Schwerdtfeger and A. Kummert, "A multidimensional signal processing approach to wave digital filters with topology-related delay-free loops," in *IEEE International Conference on Acoustics, Speech and Signal Processing (ICASSP)*, May 2014, pp. 389–393.

[34] ——, "A multidimensional approach to wave digital filters with multiple nonlinearities," in *22nd European Signal Processing Conference (EUSIPCO)*, Sept. 2014, pp. 2405–2409.

[35] A. Bernardini, P. Maffezzoni, L. Daniel, and A. Sarti, "Wave-based analysis of large nonlinear photovoltaic arrays," *IEEE Transactions on Circuits and Systems I: Regular Papers*, vol. 65, no. 4, pp. 1363–1376, Apr. 2018.

[36] S. D'Angelo and V. Välimäki, "Generalized Moog ladder filter: Part I – Linear analysis and parameterization," *IEEE/ACM Trans. on Audio, Speech and Language Processing*, vol. 22, no. 12, pp. 1825–1832, Dec. 2014.

[37] F. Fontana and M. Civolani, "Modeling of the EMS VCS3 voltage-controlled filter as a nonlinear filter network," *IEEE Trans. on Audio, Speech and Language Processing*, vol. 18, no. 4, pp. 760–772, 2010, special Issue on Virtual Analog Audio Effects and Musical Instruments.

[38] R. Bapat, *Graphs and Matrices*, ser. Universitext. London, UK: Springer, 2014.

[39] Y. Saad, *Iterative Methods for Sparse Linear Systems: Second Edition*, ser. Other Titles in Applied Mathematics. Society for Industrial and Applied Mathematics, 2003.

[40] R. A. Brualdi and D. M. Cvetković, *A Combinatorial Approach to Matrix Theory and Its Applications*. Boca Raton, FL, USA: CRC Press, 2009.

[41] R. A. Horn and C. R. Johnson, *Matrix Analysis*, 2nd ed. New York, NY, USA: Cambridge University Press, 2012.

[42] W. Rudin, *Principles of Mathematical Analysis*, 3rd ed. McGraw-Hill,, 1976.

[43] T. Schwerdtfeger and A. Kummert, "Newton's method for modularity-preserving multidimensional wave digital filters," in *IEEE 9th International Workshop on Multidimensional (nD) Systems (nDS)*, Vila Real, Portugal, Sept. 2015.

[44] K. J. Werner, V. Nangia, J. O. Smith III, and J. S. Abel, "Resolving wave digital filters with multiple/multiport nonlinearities," in *Proc. Conf. on Digital Audio Effects (DAFX-15)*, Trondheim, Norway, Nov. 2015, pp. 387–394.

[45] S. Zambon and F. Fontana, "Efficient polynomial implementation of the EMS VCS3 filter model," in *Proc. Conf. on Digital Audio Effects (DAFX-11)*, Paris, France, Sept. 2011, pp. 287–290.

[46] R. Hoffmann-Burchardi, "Digital simulation of the diode ring modulator for musical applications," in *Proc. Conf. on Digital Audio Effects (DAFX-08)*, Espoo, Finland, Sept. 2008, pp. 165–168.

[47] A. Bernardini, K. J. Werner, P. Maffezzoni, and A. Sarti, "Wave digital modeling of the diode-based ring modulator," in *Audio Engineering Society Convention 144*. Milan, Italy: Audio Engineering Society, May 2018, conv. paper #10015. Available: http://www.aes.org/e-lib/browse.cfm?elib=19411

[48] M. J. Olsen, K. J. Werner, and J. O. Smith, "Resolving grouped nonlinearities in wave digital filters using iterative techniques," in *Proc. Conf. on Digital Audio Effects (DAFX-16)*, Brno, Czech Republic, Sept. 2016, pp. 279–286.

PLACE PHOTO HERE

Federico Fontana (SM11) received the Laurea degree in electronic engineering from the University of Padova, Italy, in 1996 and the Ph.D. degree in computer science from the University of Verona, Italy, in 2003. During the Ph.D. degree studies, he was a Research Consultant in the design and realization of real-time audio DSP systems. He is currently an Associate Professor in the Department of Mathematics, Computer Science and Physics, University of Udine, Italy, teaching Auditory & tactile interaction and Computer architectures. In 2001, he was Visiting Scholar at the Laboratory of Acoustics and Audio Signal Processing, Helsinki University of Technology, Espoo, Finland. His current interests are in interactive sound processing methods and in the design and evaluation of musical interfaces. Professor Fontana coordinated the EU project 222107 NIW under the FP7 ICT-2007.8.0 FET-Open call from 2008 to 2011. Since 2017, he is Associate Editor of the IEEE TRANSACTIONS ON AUDIO, SPEECH, AND LANGUAGE PROCESSING.

PLACE PHOTO HERE

Enrico Bozzo received the Laurea degree in computer science from the University of Udine, Italy, in 1990 and the Ph.D. degree in computer science from the University of Pisa, Italy, in 1994. He is currently an Assistant Professor in the Department of Mathematics, Computer Science and Physics, University of Udine, teaching numerical analysis. He was a team member in several national research projects. His current interests are in numerical linear algebra, in particular matrix theory and its applications.

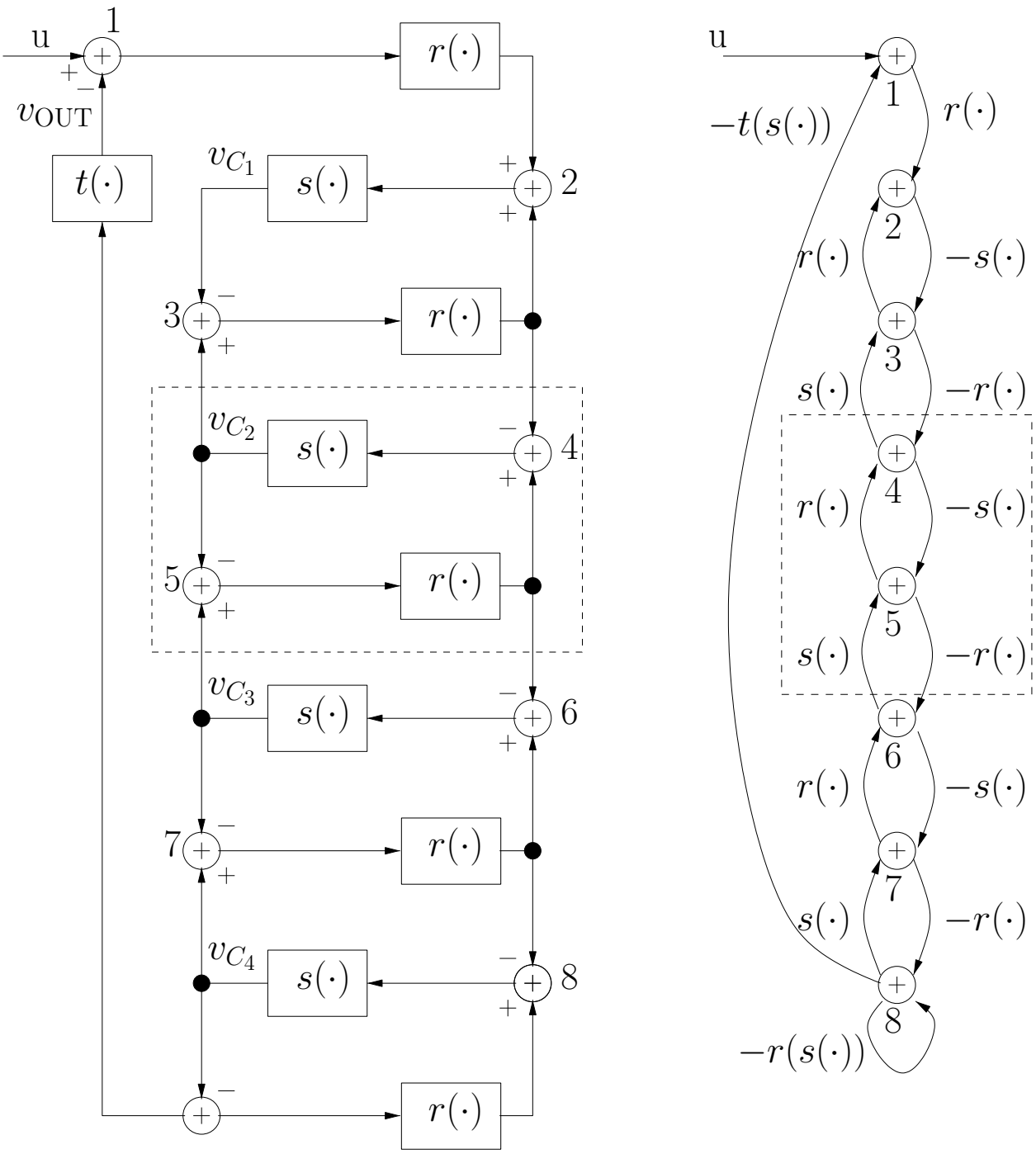

Fig. 3. VCS3 VCF network model (left) and its graph (right). One ladder element in the network and its counterpart in the graph are surrounded by a rectangle in dashed line.

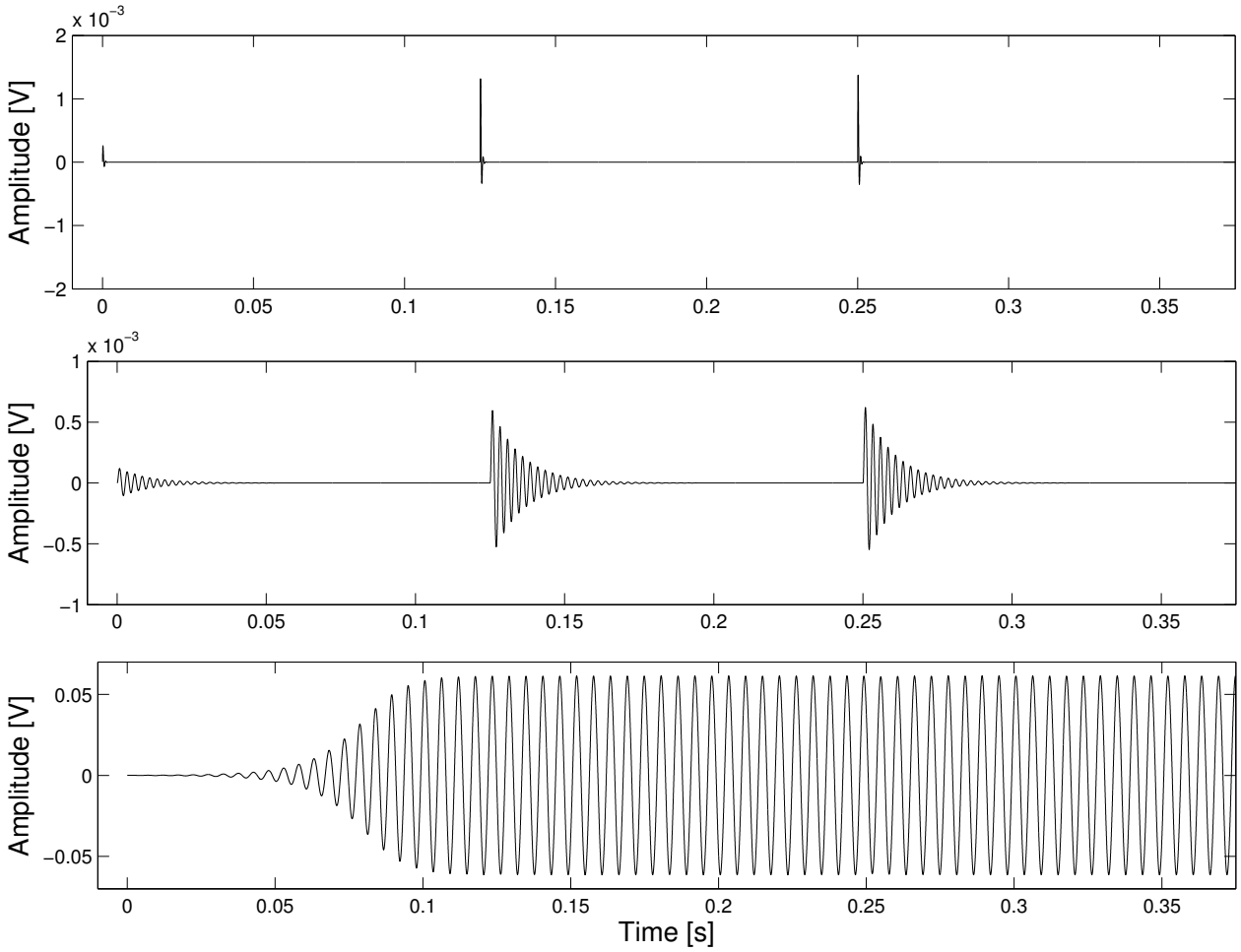

Fig. 4. Responses of a two-element (above), four-element (center), and six-element (below) ladder VCS3 VCF to a sequence of three voltage impulses respectively measuring 10 mV, 100 mV and 1 V. In all filters I_0 sets the VCF center frequency to 400 Hz and K is set to 4.

$$\boldsymbol{J}_{\mathrm{VCF}}(\boldsymbol{\Xi}) = \begin{bmatrix} 0 & 0 & 0 & 0 & 0 & 0 & 0 & -s'(\xi_{1,8})t'(s(\xi_{1,8})) \\ r'(\xi_{2,1}) & 0 & r'(\xi_{2,3}) & 0 & 0 & 0 & 0 & 0 \\ 0 & -s'(\xi_{3,2}) & 0 & s'(\xi_{3,4}) & 0 & 0 & 0 & 0 \\ 0 & 0 & -r'(\xi_{4,3}) & 0 & r'(\xi_{4,5}) & 0 & 0 & 0 \\ 0 & 0 & 0 & -s'(\xi_{5,4}) & 0 & s'(\xi_{5,6}) & 0 & 0 \\ 0 & 0 & 0 & 0 & -r'(\xi_{6,5}) & 0 & r'(\xi_{6,7}) & 0 \\ 0 & 0 & 0 & 0 & 0 & -s'(\xi_{7,6}) & 0 & s'(\xi_{7,8}) \\ 0 & 0 & 0 & 0 & 0 & 0 & -r'(\xi_{8,7}) & -s'(\xi_{8,8})r'(s(\xi_{8,8})) \end{bmatrix} \tag{19}$$

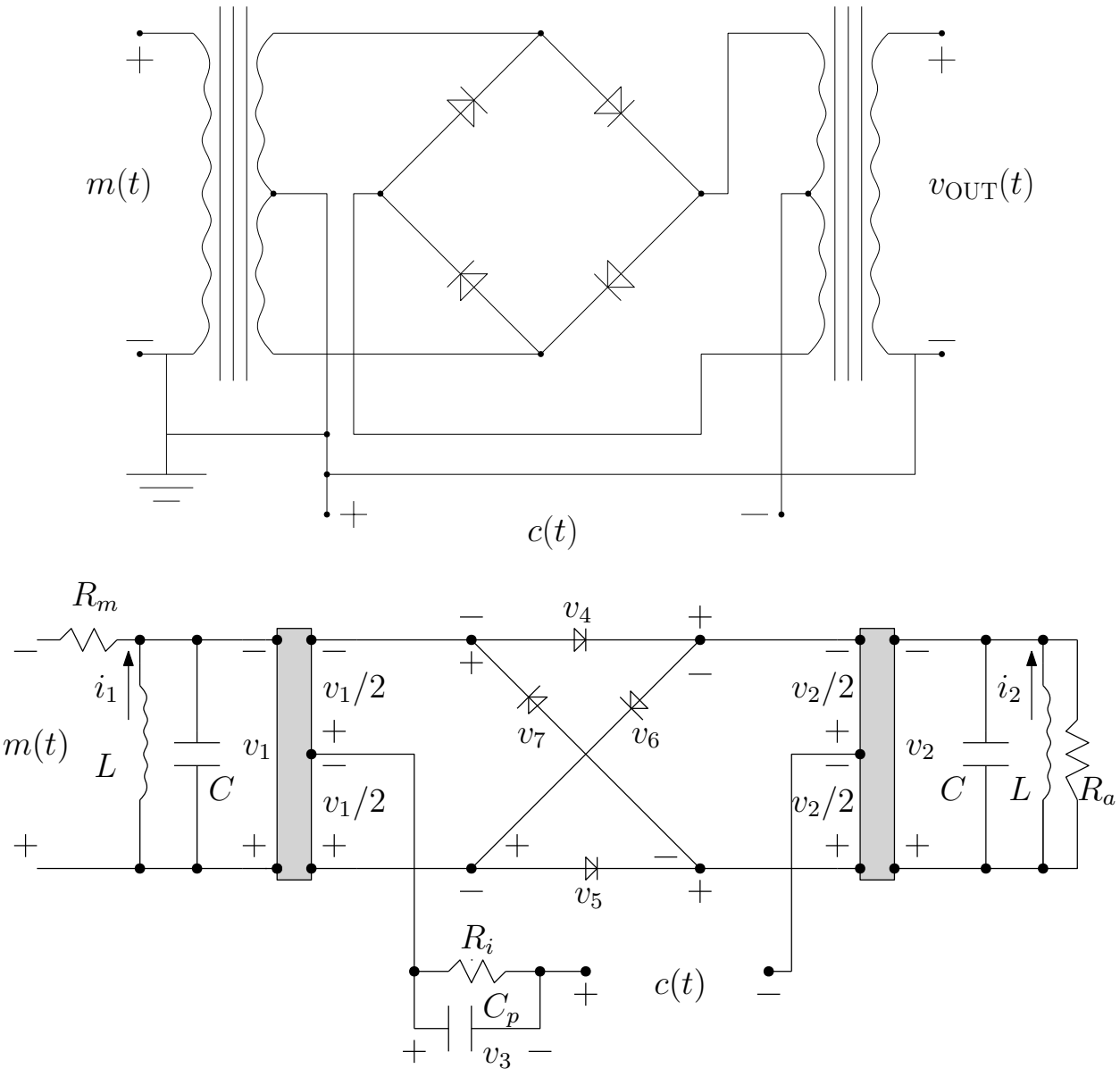

Fig. 5. Ring modulator circuit (above) and analogue model (below) [46].

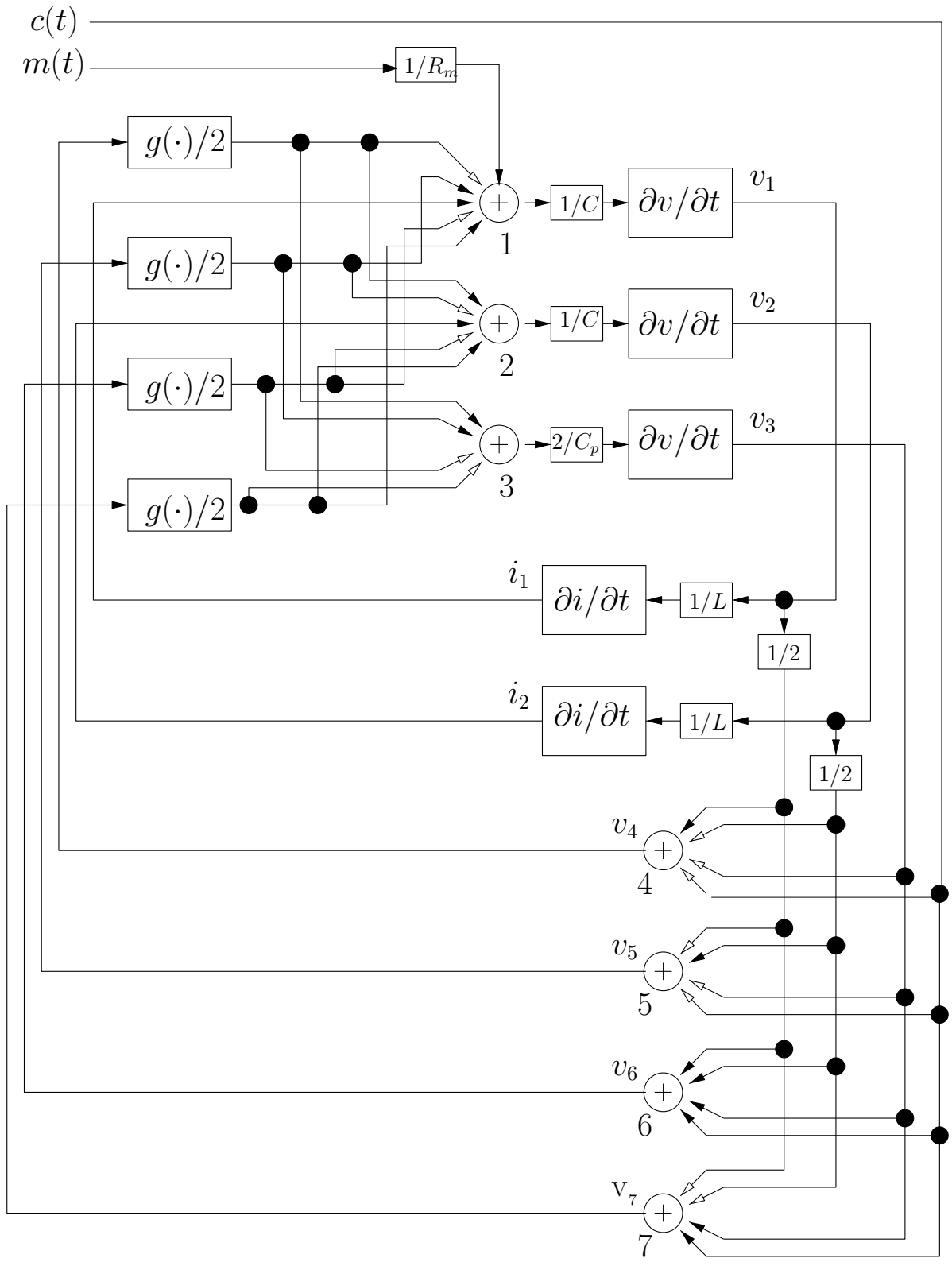

Fig. 6. Filter network model of the ring modulator. The feedback chain forms the lower part of the network. Black arrows add, whereas white arrows subtract the incoming component to the summation block.

$$\boldsymbol{J}_{\mathrm{RM}}(\boldsymbol{\Xi}) = \begin{bmatrix} 0 & 0 & 0 & -\frac{\rho_m g'(\xi_{1,4})}{2} & \frac{\rho_m g'(\xi_{1,5})}{2} & -\frac{\rho_m g'(\xi_{1,6})}{2} & \frac{\rho_m g'(\xi_{1,7})}{2} & \rho_m & 0 \\ 0 & 0 & 0 & \frac{\rho_a g'(\xi_{2,4})}{2} & -\frac{\rho_a g'(\xi_{2,5})}{2} & -\frac{\rho_a g'(\xi_{2,6})}{2} & \frac{\rho_a g'(\xi_{2,7})}{2} & 0 & \rho_a \\ 0 & 0 & 0 & \rho_i g'(\xi_{3,4}) & \rho_i g'(\xi_{3,5}) & -\rho_i g'(\xi_{3,6}) & -\rho_i g'(\xi_{3,7}) & 0 & 0 \\ 1/2 & -1/2 & -1 & 0 & 0 & 0 & 0 & 0 & 0 \\ -1/2 & 1/2 & -1 & 0 & 0 & 0 & 0 & 0 & 0 \\ 1/2 & 1/2 & 1 & 0 & 0 & 0 & 0 & 0 & 0 \\ -1/2 & -1/2 & 1 & 0 & 0 & 0 & 0 & 0 & 0 \\ -\frac{\mu}{LF_s} & 0 & 0 & 0 & 0 & 0 & 0 & 0 & 0 \\ 0 & -\frac{\mu}{LF_s} & 0 & 0 & 0 & 0 & 0 & 0 & 0 \end{bmatrix} \tag{23}$$

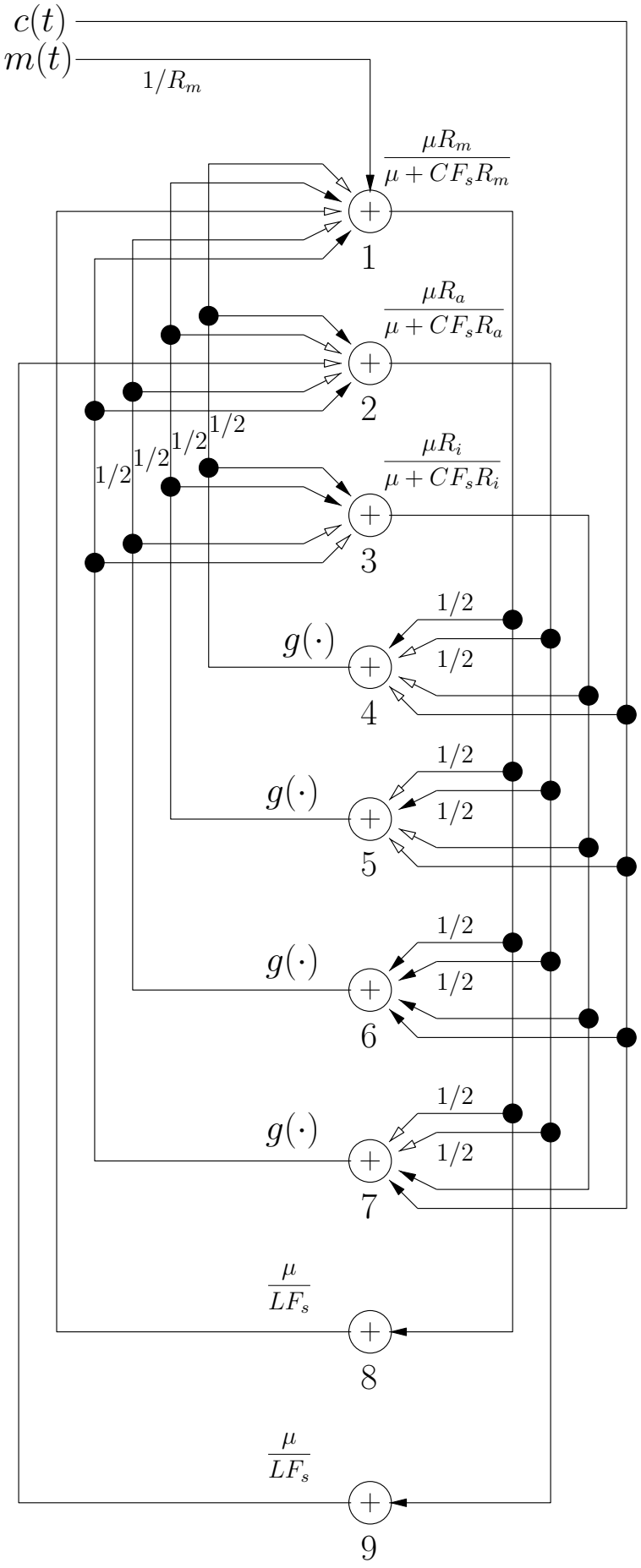

Fig. 7. Graph of the ring modulator implicit models. Nodes $k = 1, \ldots, 7$ refer to the respective voltage v_k. Nodes 8 and 9 host

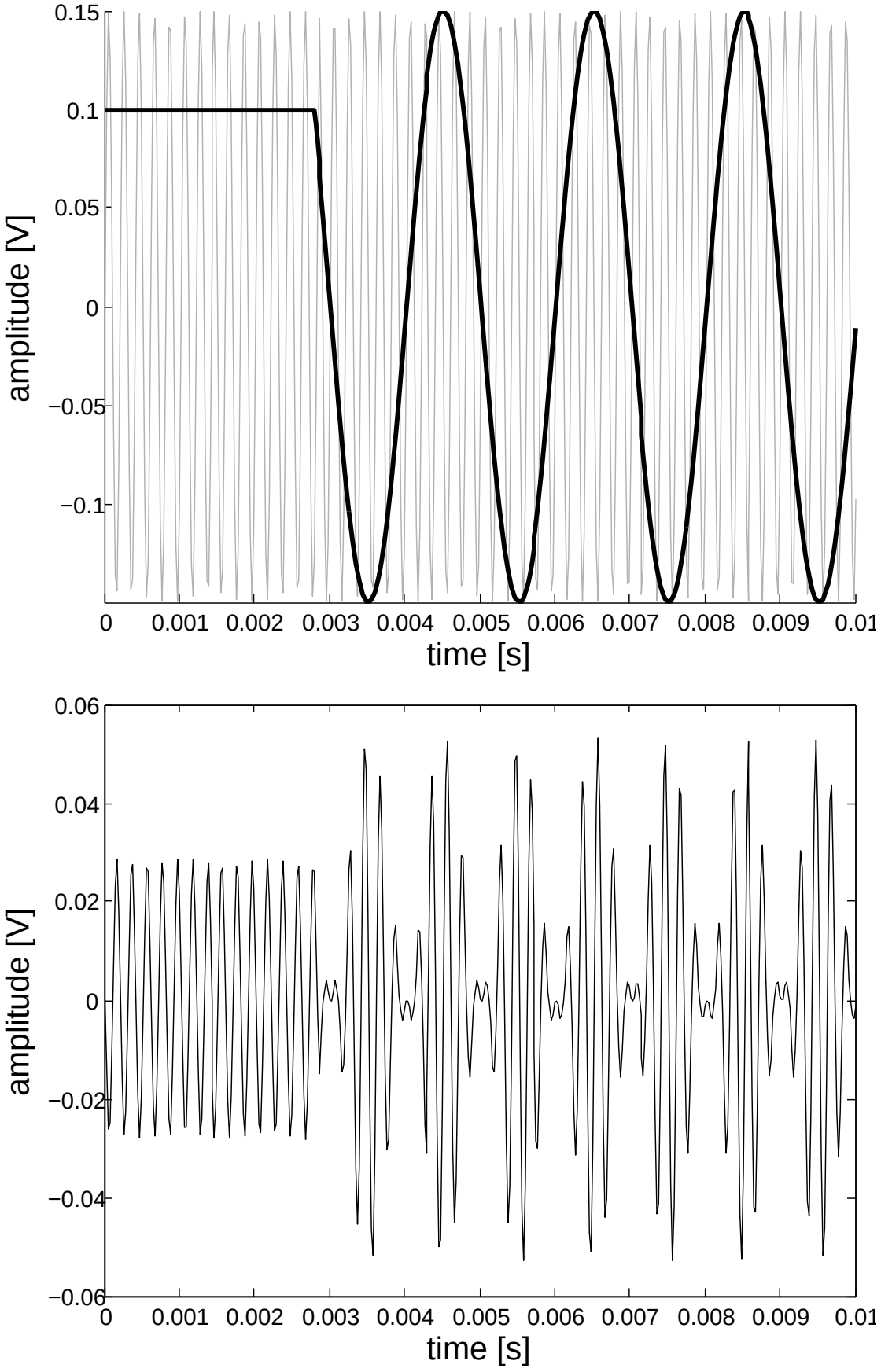

Fig. 8. Ring modulator. Above: modulator (thin gray line) and carrier (thick black line) input signals, first 10 ms. Below: output signal with backward Euler discretization, first 10 ms.

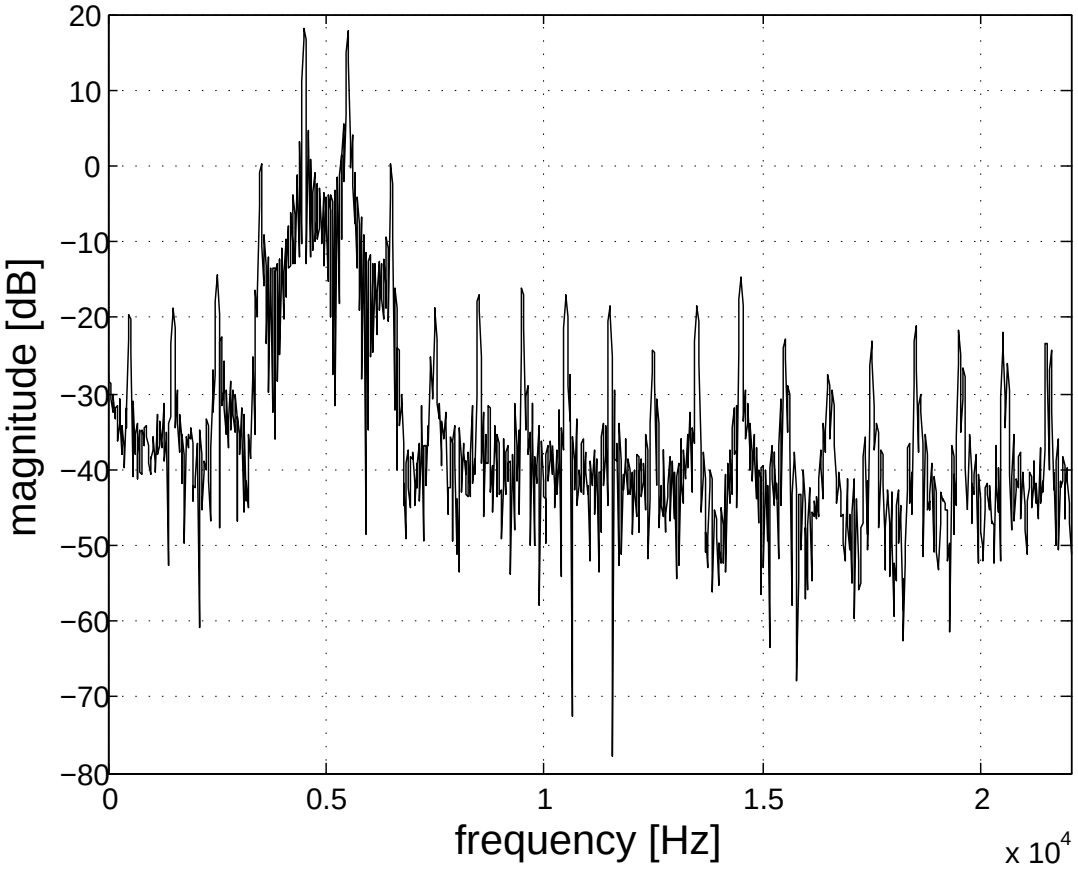

Fig. 9. Ring modulator. Spectrum until $F_s/2$ of the amplitude-modulated signal portion in Fig. 8, first 200 ms.

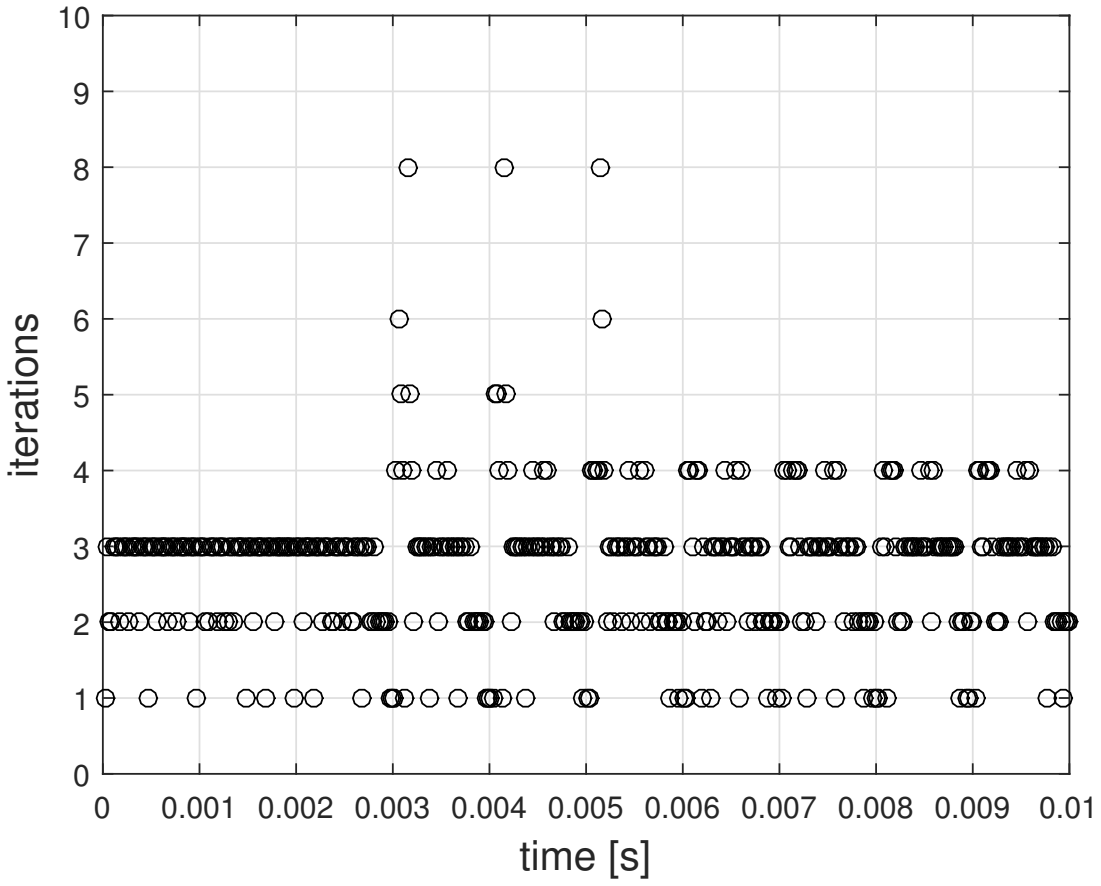

Fig. 10. Ring modulator. Number of iterations at each temporal step during the fixed-point search leading to Fig. 8.

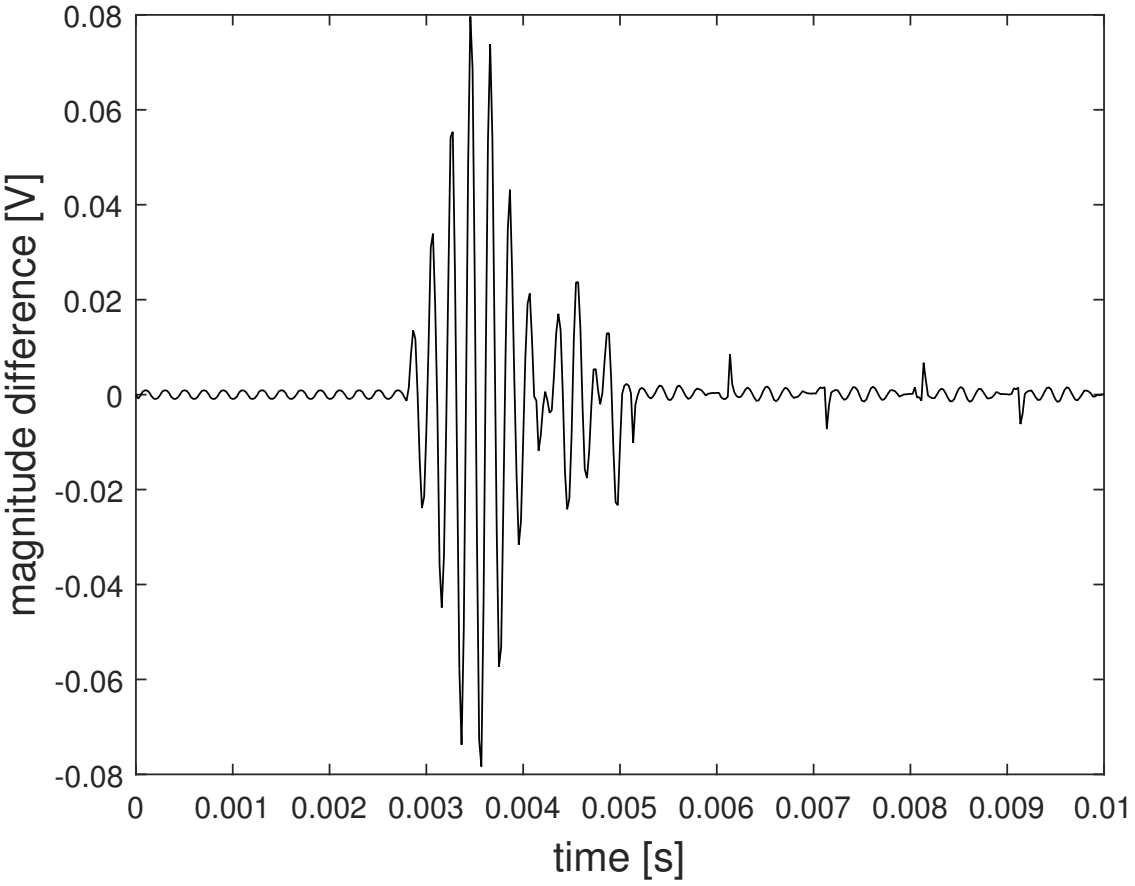

Fig. 11. Ring modulator. Difference between the explicit and fixed-point solution leading to Fig. 8, first 10 ms.